Importance of growth method and substrate-induced crystalline quality in $Al/Gd_{0.2}Ca_{0.8}MnO_3/Au$ memristor devices

I. Angervo[1], A. Antola[1], T. Vaimala[1], A. Malmi[1,2], A. Schulman[1,3,*], H. Huhtinen[1] and P. Paturi[1]

[1] Wihuri Physical Laboratory, Department of Physics and Astronomy, FI-20014 University of Turku, Finland

[2] University of Turku Graduate School (UTUGS), University of Turku, FI-20014 Turku, Finland

[2] Department of Chemistry, FI-20014 University of Turku, Finland

[3] Facultad de Ciencias, Universidad de Salamanca, 37008 Salamanca, Spain

E-mail: schulman@usal.es

Abstract.

We report on the impact of the growth method and substrate-induced crystalline quality on the performance of planar $Al/Gd_{0.2}Ca_{0.8}MnO_3/Au$ memristor devices. Structural, magnetic, and resistive properties were thoroughly examined for fundamental characterizations, with a particular emphasis on their correlation with the memristive properties of fabricated devices. Our findings suggest that memristor structures grown on single crystal $SrTiO_3$ substrates using pulsed laser deposition consistently exhibit superior crystalline quality compared to those fabricated using chemical solution deposition and on silicon-based substrates. Despite variations in growth method and substrate, all memristor structures display typical resistive switching behaviour, distinguishing between high-resistance and low-resistance states. However, endurance and retention measurements demonstrate that memristor structures produced via pulsed laser deposition on single crystalline $SrTiO_3$ demonstrate the most favourable resistive switching properties. To elucidate the mechanisms underlying the differences in resistive switching behavior across substrates and deposition methods, we extensively discuss these issues in the context of structural distortion and conduction mechanisms.

1. Introduction

As technology continues to advance at an astonishing pace, the need for faster and more efficient memory technologies has become increasingly crucial [1, 2, 3, 4]. One promising next-generation memory device is the so-called memristor or resistive random access memory (RRAM), which utilizes materials capable of switching between high and low resistance states upon the application of electrical pulses. [5, 6, 7, 8]. The advantages of RRAM and its potential applications in emerging technologies such as artificial intelligence or neuromorphic devices and computer architectures are undeniable. These include, but are not limited to, new nonvolatile memory systems, the removal of von Neumann bottleneck and hysteretic multilevel resistance states, valuable for neuromorphic computing. [9, 10, 11, 12]. However, numerous challenges still need to be addressed to identify optimal materials and appropriate manufacturing techniques for practical and commercially viable technologies.

Memristor devices are comprised of a simple structure with a material with a switchable resistance through a process called resistive switching (RS), which works as a storage medium, between two metal electrodes [13]. The switching layer can be composed of simple oxides such as AlO_x [14], HfO_2 [15], TaO_2[16], or more complex oxides like the so-called perovskites structure materials (*e.g.* manganites, titanates, cobaltites, etc) [17, 18], which are particularly intriguing due to their intrinsic forming-free behavior and quasi-continuous resistive modulation. This analog-like behavior renders perovskite memristors, particularly those of the manganite family, highly adaptable for neuromorphic computing tasks and synaptic emulation, offering potential advantages in terms of energy efficiency and computational precision.

Manganite-based memristor devices, which have a switching layer consisting of manganite oxides such as $La_{1-x}Sr_xMnO_3$ (LSMO), $La_{1-x}Ca_xMnO_3$ (LCMO), $Gd_{1-x}Ca_xMnO_3$ (GCMO) and $Pr_{1-x}Ca_xMnO_3$ (PCMO), all exhibit unique electronic and magnetic properties although they present similar memristive behavior [19, 17, 20, 21, 22, 23]. As the switching layer of memristor devices, they have shown to have small device-to-device variability, forming-less operation, and well-controlled analog resistance states, gaining them attention as a promising material family for memory and neuromorphic applications with crossbar arrays. In particular, we chose GCMO as the intermediate layer of the device due to its unique properties., GCMO has recently emerged as an intriguing candidate among the mixed-valence manganites due to its charge and orbital ordered state (CO/OO) and insulator-to-metal transition (IMT) near room temperature [24, 25, 26, 27]. In addition to these properties, GCMO exhibits a high degree of tunability in its electronic properties with calcium doping. At a high calcium doping range, GCMO not only exhibits similar memristive properties to more commonly reported materials like PCMO, but in some cases, it surpasses them [23]. One of the key advantages of GCMO is its elevated interface resistance in the memristor device. This results in reduced energy consumption, making GCMO-based devices more energy-efficient. Furthermore, the high interface resistance also leads to reduced detrimental

leakage currents in crossbar array architectures [28, 23, 29]. This could be a significant advantage in the design of memristor devices, where leakage currents can lead to cross-talk and other unwanted effects.

Therefore, GCMO-based resistive switching memristors present a promising alternative to existing memristor technologies and have the potential to revolutionize the field of electronics.

However, manufacturing manganite thin films for interface-type RRAMs is a challenging task, particularly when using pulsed laser deposition (PLD), which has limitations when it comes to coating large areas. To overcome this issue, a new process based on citrate-based aqueous chemical solution deposition (CSD) has been developed for GCMO [30]. This process is environmentally friendly and capable of producing high-quality GCMO thin films, suitable for memristor applications integrated into large silicon wafers. However, achieving the same crystal structure and RS properties as PLD-produced films presents a challenging task. Achieving this, requires optimizing the chemical process, identifying the correct substrate or buffer layer material, and determining the optimal heat treatment process.

In this work, we systematically investigated the impact of growth methods, specifically pulsed laser deposition and chemical solution deposition, on the production of high-quality mixed-valence GCMO perovskite memristors for resistive switching-based memory technologies. We also examined the role of substrate-induced crystalline nature in this process by comparing the growth of GCMO on single crystal $SrTiO_3$ and, on the other hand, on Si wafer having thin epitaxially grown $SrTiO_3$ layer on the top. Through detailed structural analysis using X-ray diffractometry, as well as magnetic and resistive switching measurements, we discovered controllable properties that could be exploited in future GCMO-based memory devices integrated with silicon wafers.

2. Experimental details

The $Al/Gd_{0.2}Ca_{0.8}MnO_3/Au$ memristive structures (hereafter Al/GCMO/Au) were deposited on two different substrates by two deposition methods. The substrates utilized are (1) one-side polished $SrTiO_3$ (hereafter STO) (100) single crystal substrates from Crystal GmbH with an orientation accuracy $<0.5^\circ$ and micro-roughness <0.5 nm and (2) a Si wafer (Lumiphase Corporation), where a 4 nm thick epitaxial $SrTiO_3$ layer with surface roughness <0.5 nm and mosaicity of $<0.4^\circ$ was deposited (hereafter Si/STO). We performed atomic force microscopy (AFM) measurements (Bruker Innova®) to confirm that both the single crystal STO and Si/STO bilayer substrates are almost atomically flat, with average surface RMS roughnesses 0.22 nm and 0.28 nm, respectively. The AFM images of both substrates STO (a) and Si/STO (b) together with the schematic illustrations of the GCMO and substrate materials (c) are given in Fig. 1. To study the effect of the growth method, in addition to traditionally used pulsed laser deposition (PLD) [25, 26, 23] , films were also grown using a citrate-based aqueous chemical solution deposition (CSD) method [30].

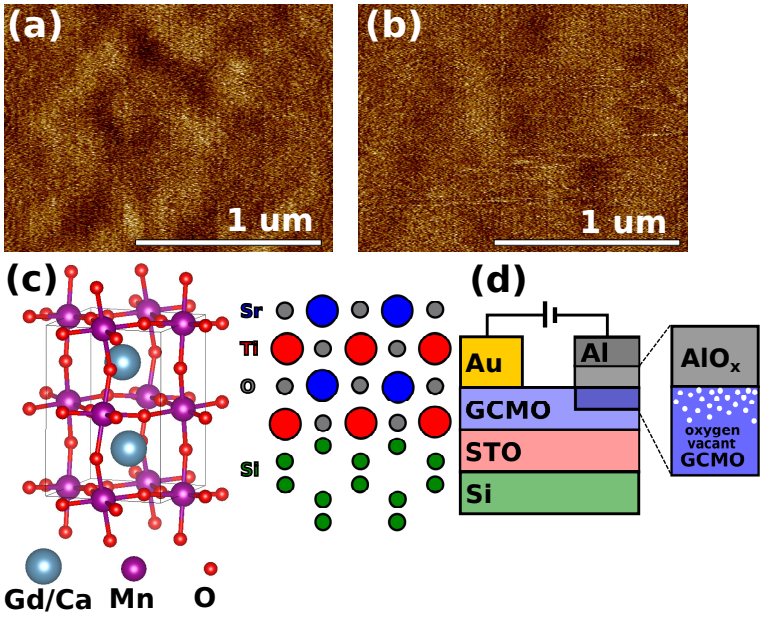

Figure 1: The surface microstructure measured by AFM for (a) single crystal STO and (b) Si/STO (b) substrates using $2\times2\,\mu m^2$ scan area. (c) schematic illustration of GCMO unit cell together Si(001)/STO(100) bilayer substrate. (d) A planar Al/$Gd_{0.2}Ca_{0.8}MnO_3$/Au memristor device configuration, where the active AlO_x switching interface is formed due to the oxygen released from the GCMO.

In the PLD process, polycrystalline GCMO targets synthesized in-house by solid-state method [31] were used by applying 2000 pulses of XeCl laser (λ = 308 nm) with energy fluence of 1.6 J/cm^2 and repetition rate of 5 Hz. The ablation temperature during the deposition was 700 °C, after which the films were *in situ* post-annealed at 700 °C for 10 min in oxygen atmosphere, before cooling them down to room temperature. The details of the PLD device and the deposition process have been reported elsewhere [32, 33]. For the CSD films, one layer of the precursor solution corresponding to GCMO x=0.8 [30] was first spin-coated on clean and hydrophilic STO and Si/STO substrates at 5000 rpm in air. The combined drying and pyrolysis was done in an oven at 350 °C for 3 h, using heating and cooling ramps of 0.5°/min. The final crystallization of the GCMO phase was obtained in a furnace at 750 °C for 24 h in flowing oxygen. From now on, the abbreviations PLD_{STO}, $PLD_{Si/STO}$, CSD_{STO} and $CSD_{Si/STO}$ will be used for the names of the samples, related to the manufacturing method and the substrate material used. The thicknesses of the films as measured over the stripe edge by AFM were approximately 80 nm, 80 nm, 180 nm and 180 nm for PLD_{STO}, $PLD_{Si/STO}$, CSD_{STO} and $CSD_{Si/STO}$, respectively.

The crystalline quality of the films was studied by X-ray diffractometry (XRD) using PANalytical Empyrean diffractometer in Bragg-Brentano mode. Temperature-dependent zero-field-cooled (ZFC) and field-cooled (FC) magnetizations were measured at temperatures between 10 K and 400 K with a Quantum Design MPMS XL

magnetometer in 50 mT magnetic field. The magnetic hysteresis loops were collected at 10 K in a field up to 5 T, being parallel to the film plane i.e. along the GCMO ⟨110⟩ direction. The temperature-dependent resistivities were measured with a standard four-probe method using the current 0.5 μA in Quantum Design physical property measurement system (PPMS).

In addition, resistive switching properties of Al/GCMO/Au in a planar configuration were characterized using a Keithley 2614b Source/Meter by measuring pulsed $I-V$ loops at room temperature. After each write pulse in the $I-V$, a small read voltage of 0.2 V in amplitude and 50 ms in width was applied to obtain remnant resistance values i.e. R_{probe}. This type of curve is called resistance hysteresis switching loops (RHSL) and provides a clear view of the behavior of the non-volatile resistance of the devices as well as accumulation effects, since we are in fact accumulating pulses of the same polarity. The RSHL are fabricated by plotting the upon the R_{probe} measured at V_{read} against the last applied writing pulse V. Thus, R_{probe} and R are only equal when V = V_{read}

To obtain reliable high and low resistance states (HRS and LRS, respectively) and thus the maximal switching ratio, 50 cycles were applied by varying the voltage range between the values V_{min} and V_{max}. The retention and endurance measurements of the devices were measured using an ArcONE Memristor Characterization Platform by ArC Instruments™. As schematically illustrated in Fig. 1(d), the Au electrodes were deposited on top of the GCMO film using an E-beam evaporator of Elettrorava S.p.A. and an active Al interface producing AlO_x barrier layer between Al and GCMO was implemented by wiring another electrode on the GCMO surface using a TPT HB05 Wire Bonder with a 33 μm diameter aluminum wire.

3. Results

3.1. Microstructure and crystalline quality caused by substrate and growth method

Based on the XRD $\theta-2\theta$ diffractograms, the films are phase pure. Regardless of the deposition method or substrate, they grow with the GCMO (00l) peaks along the out-of-plane direction of the film. The pole figures of the texture scans for the GCMO (204) reflections in Fig. 2(a) reveal four relatively sharp maxima at 90° intervals in films deposited by CSD on both STO and Si/STO substrates. This indicates good in-plane ordering, high crystallinity, and epitaxy.

We identified the positions of the GCMO peaks and their full widths at half maxima (FWHM) by fitting the peaks with a pseudo-Voigt function. The obtained lattice parameters are shown in Table 1 and they do not significantly change with either growth method or substrate material. Moreover, they closely resemble either the nominal values or the measurements observed for the polycrystalline bulk GCMO samples, such as a=5.29 Å and b=5.33 Å [24]. However, these dimensions are notably smaller than the in-plane lattice parameters of the STO (5.52 Å along the diagonal), suggesting the presence

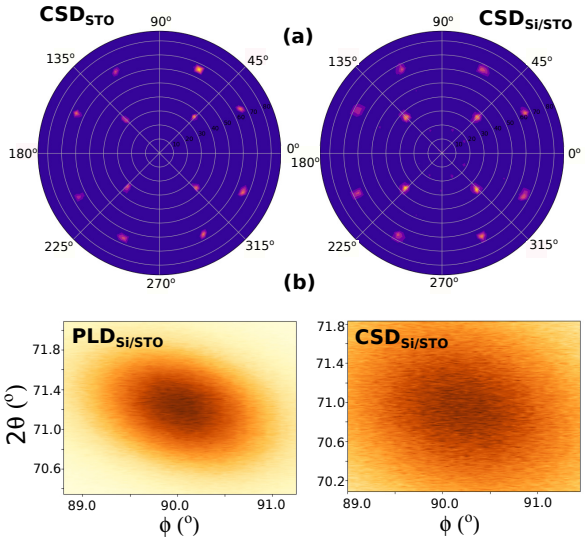

Figure 2: (a) The pole figures of the texture scans with relative intensities for (204) peaks of GCMO deposited by CSD on STO and Si/STO substrates. (b) GCMO (224) peaks as a function of 2θ and ϕ for PLD and CSD deposited films on Si/STO substrates.

Table 1: Structural properties such as unit cell parameters, cell volume, FWHM widths of the XRD peaks and the thickness of the films determined from the room temperature XRD and AFM data.

Sample	a (Å)	b (Å)	c (Å)	V_{cell} (%)	$\Delta\theta_{004}$ (°)	$\Delta\phi_{204}$(°)	d (nm)
PLD_{STO}	5.28	5.33	7.49	210.6	0.4505	1.79	80
$\text{PLD}_{\text{Si/STO}}$	5.29	5.33	7.46	210.2	0.2109	1.97	80
CSD_{STO}	5.31	5.29	7.48	209.9	0.4627	2.12	180
$\text{CSD}_{\text{Si/STO}}$	5.26	5.23	7.36	202.4	0.4839	3.36	180

of tensile strain during the initial growth stages. When examining the peak widths in the 2θ-direction, the PLD film grown on a Si/STO substrate exhibits much narrower peaks than respective films grown on STO. This suggests that the strain in $\text{PLD}_{\text{Si/STO}}$ relaxes much faster than in single crystal STO.

Moreover, a larger structural in-plane variation in CSD-grown films is evidenced by the significantly broader ϕ peaks, as can be observed in Fig. 2(b) and in Table 1. These findings indicate a considerable amount of low-angle grain boundaries in $\text{CSD}_{\text{Si/STO}}$, resulting in strain relaxation of GCMO. Coincidentally, the thin film produced with CSD and grown on a Si/STO substrate has the smallest lattice parameters in all directions, leading to a significantly smaller unit cell volume.

3.2. Differences in magnetic and resistive transitions

The magnetic transitions of the PLD_{STO}, $\text{PLD}_{\text{Si/STO}}$, CSD_{STO}, and $\text{CSD}_{\text{Si/STO}}$ samples were investigated by measuring the zero-field-cooled (ZFC) and field-cooled (FC)

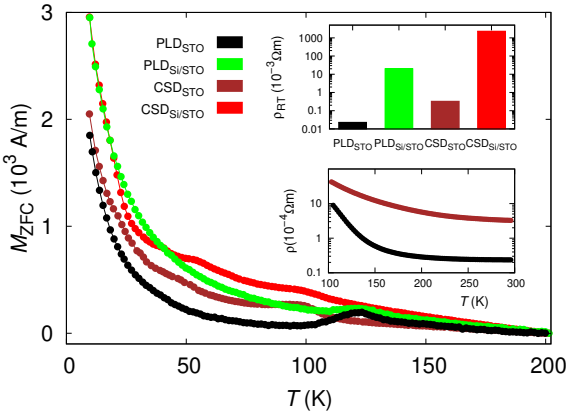

Figure 3: Temperature dependence of the zero-field-cooled (ZFC) magnetization of GCMO measured in 50 mT field for PLD_{STO}, $PLD_{Si/STO}$, CSD_{STO}, and $CSD_{Si/STO}$ samples (main panel). The lower inset exemplarily shows the temperature-dependent resistivities of the same samples, whereas the inset on the top illustrates how the room temperature resistivities ρ_{RT} vary within all the samples. The resistances of the samples grown on Si/STO samples are too high, and thus the complete temperature dependence could not be measured.

magnetizations in the temperature range of 10–400 K at a field of 50 mT. Additionally, to clarify the differences in remanent magnetizations as well as in coercivity fields, the magnetic hysteresis loops were measured up to 2.5 T at temperatures of 10 K and 300 K, results that are summarized in Table 2. The ZFC curves for all samples are shown in the main panel of Fig. 3. From the figure, it is evident that all the samples exhibit a complex magnetic behaviour with a mixture of competing ferromagnetic (FM) and antiferromagnetic (AFM) states, which can be attributed to the FM double exchange interaction between Mn^{3+} and Mn^{4+} ions in the non-ferromagnetic matrix, as well as the AFM superexchange interaction between Mn^{3+}-Mn^{3+} and Mn^{4+}-Mn^{4+} pairs [34, 35]. The magnetic ordering temperature, T_N, was estimated from the $M(T)$ curves by determining the minimum of the derivative, dM/dT. As shown in Table 2, T_N is approximately 25 K lower in films prepared by CSD compared to PLD films, regardless of the substrate material utilized. The small peak observed in the ZFC curves below T_N can be attributed to spin-glass behaviour resulting from the competition between FM and AFM interactions [25]. Furthermore, as indicated in Table 2, the remanent magnetization is smaller and the coercivity field is greater in films grown by CSD compared to those deposited by PLD. This can be linked to the greater number of low-angle grain boundaries that can pin the domain walls [36, 37], or to the different spin rotation between AFM and FM coupled domains [38, 39].

To study the temperature dependence of resistance temperature, Au stripes were evaporated on the two edges of the GCMO samples. Results for STO samples are shown in the lower inset of Fig. 3, the resistivity levels and shapes of the $R(T)$ curves

Table 2: Essential magnetic and electric properties of the samples: Néel temperature T_N, remanent magnetization M_{Rem}, coercive field B_c and the resistivity measured at room temperature ρ_{RT}.

Sample	T_N (K)	M_{Rem} (10^3 A/m)	B_c (mT)	ρ_{RT} (Ω·m)
PLD_{STO}	123	6.5	2.5	$2.3{\cdot}10^{-5}$
$PLD_{Si/STO}$	122	4.8	7	$2.0{\cdot}10^{-2}$
CSD_{STO}	96	1.4	47	$3.3{\cdot}10^{-4}$
$CSD_{Si/STO}$	99	3.0	27	2.3

exhibit significant differences among the samples. The main distinctions between the samples are summarized in the upper inset of Fig. 3 and Table 2, where differences in resistivity at room temperature can be observed. For instance, the resistivity of the GCMO film grown on PLD_{STO} measures 23 $\mu\Omega$m, whereas the same film grown on a Si/STO substrate exhibits a resistivity three orders of magnitude higher. Similarly, compared to PLD, the CSD method consistently yields higher resistance in GCMO films. As a result, the GCMO film grown on $CSD_{Si/STO}$ displays a significantly higher resistivity of 2.3 Ωm at room temperature. This clearly indicates that the thin STO layer grown on the Si wafer considerably inhibits the in-plane growth of GCMO, rendering it insufficiently conductive to serve as a bottom electrode in the capacitive memristor structure. These resistance findings align well with our structural studies, which revealed a broadening of the ϕ-peak on the plane in $CSD_{Si/STO}$ compared to other samples.

3.3. Resistive switching properties in planar memristors

Our previous research has already shown the existence of resistive switching characteristics in GCMO, prepared both by PLD and CSD, on single crystal STO substrates [23, 30, 40]. The phenomena are again confirmed here in addition to the Si/STO substrate as well for both deposition methods as depicted in Fig. 4 (a) for PLD and (c) for CSD-prepared films on STO. Respectively prepared GCMO films on Si/STO substrates also show resistive switching, which can be seen from Fig. 4 (b) and (d).

In Figure 4, we present the resistive switching results for PLD_{STO}, $PLD_{Si/STO}$, CSD_{STO} and $CSD_{Si/STO}$. The $R-V$ (red) and $R_{probe}-V$ (blue) curves illustrate the distinct behaviors for the write and read pulses, respectively. For PLD_{STO} (a), a stable resistive switching with a difference between high (HRS) and low (LRS) resistance states of around one order of magnitude. This contrasts with the behavior of $PLD_{Si/STO}$ (b), which shows very unstable switching with a reduced hysteresis, which is calculated by the difference between the states at bias voltage (< 0.5V). It is noted that due to apparent instability in $PLD_{Si/STO}$ the bipolar nature of the RS becomes indistinct. However, in our previously published research the bipolar RS is apparent in an identical device [40]. Similarly, to what was observed in PLD, CSD_{STO} (c) demonstrates improved performance over $CSD_{Si/STO}$ (d), indicating that the STO buffer layer incorporated in the silicon substrate significantly reduces resistive

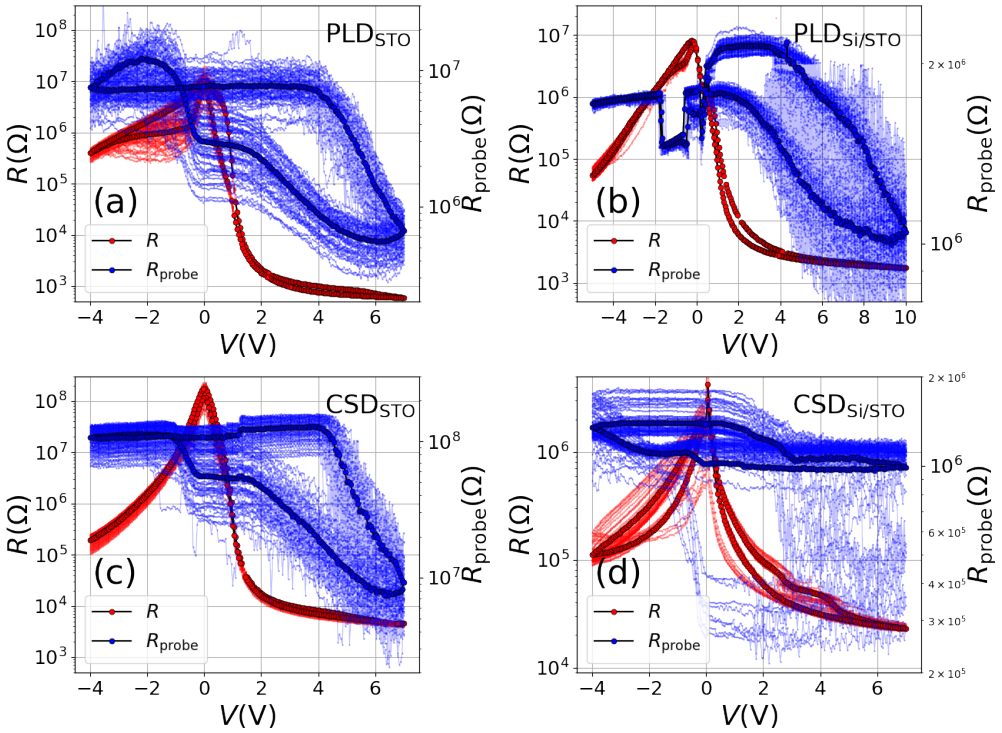

Figure 4: Resistive switching results including $R-V$ (red) probed $R_{\text{probe}}-V$ (blue) for PLD_{STO}, $\text{PLD}_{\text{Si/STO}}$, CSD_{STO}, $\text{CSD}_{\text{Si/STO}}$, respectively in (a), (b), (c) and (d).

switching characteristics, which corresponds to a decrease in the film crystal quality. These results underscore the importance of fabrication processes in the development of high-performance, multifunctional devices. There are notable differences between samples regarding the SET/RESET voltages. Indeed both devices on STO demonstrate similar well-localized voltage values above +4 V for setting the device into LRS and voltage close to -0.2 V for resetting the device back to HRS, although the SET process happens more gradually. However, $\text{CSD}_{\text{Si/STO}}$ shows gradual multi-state switching in both SET and RESET. In $\text{PLD}_{\text{Si/STO}}$ determining RESET voltage is not practical due to apparent instability but the gradual SET process above +4 V is clear. The relatively high SET voltage and the apparent asymmetry in switching are apparent characteristics, which have already been demonstrated in our manganite-based RS devices [23, 41, 30]. However, SET voltage amplitude for setting the GCMO-based device to a particular resistance state dependents on the preceding RESET voltage amplitude [30]. Applying the asymmetric voltage amplitudes with opposite polarities therefore enables analog control, demonstrated also in other systems [42, 43].

In addition to $R-V$ curves, we also investigated the effects of the crystallinity and deposition methods in other relevant memristive properties such as endurance and memory retention. Polarity alternating SET/RESET-pulses, with a low reading voltage of 0.2 V/0.4 V in between, were used to study the endurance of the resistive states in the devices. In addition, the devices were checked for their resistive state retention, in

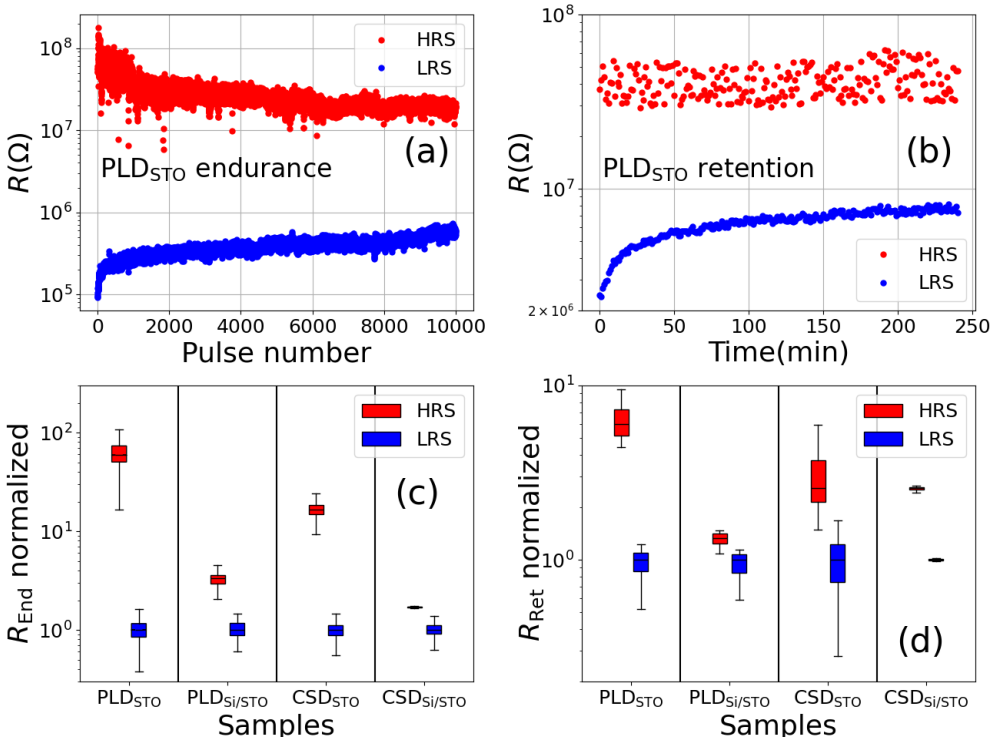

Figure 5: (a) Endurance and (b) retention results for single PLD_{STO} device. The combined and normalized endurance (c) and retention (d) results for all the samples presented as box plots. The boxes represent the quartiles of HRS and LRS stages on both sides of the median, and the whiskers depict the extreme values of the parameter.

which the device was SET/RESET by applying a set of ten voltage pulses, each pulse with 50 ms width. As an example, the respective raw results for PLD_{STO} are presented for endurance and retention in Fig. 5 (a) and (b). It is demonstrated that during the repetitive SET/RESET pulsing the resistance gap between LRS and HRS is diminished as both states move closer to an intermediate state. However, despite this the LRS and HRS states remain clearly distinctive throughout the endurance characterization. We have observed a similar phenomenon in our previously reported results on GCMO memristors [23]. The endurance results for other samples here did not reveal clear state decay toward an intermediate resistance state. Instability in the endurance was detected, as identical SET/RESET pulsing set the devices in different resistance states. In retention results, it is clear that the LRS state relaxes towards the stable HRS state, while again the LRS and HRS remain distinctive.

The collected endurance and retention results for the samples are presented in Fig. 5 (c) and (d), respectively, as box and whisker plots. The results are normalized according to LRS median for clarification. Statistically, all devices exhibit distinct LRS and HRS characteristics in both endurance and retention. However, there is a slight overlap in the extreme values of the states observed for $PLD_{Si/STO}$ and CSD_{STO} samples in the retention measurements. This is due to LRS relaxation towards the HRS state.

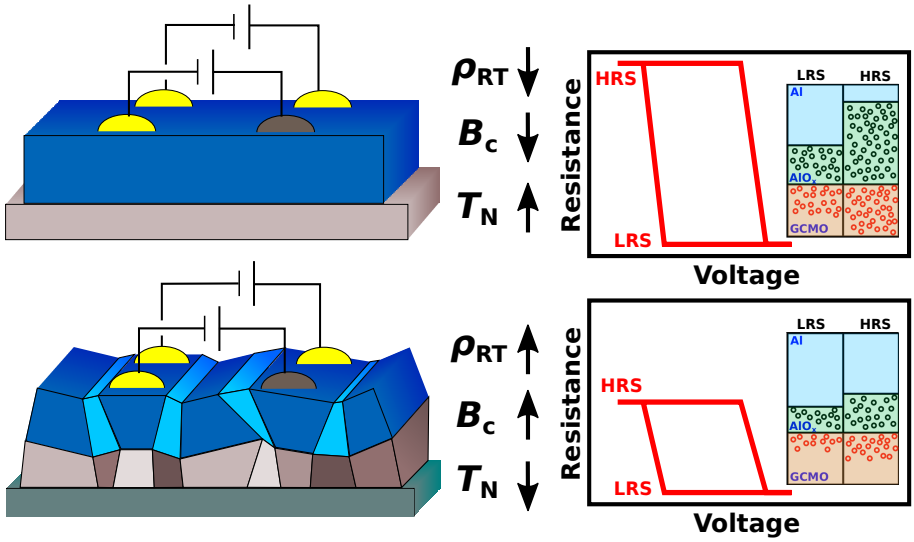

Figure 6: Schematic figure illustrating the discussion topics on structural deformation and its influences on GCMO films. Schematic films represent PLD_{STO} (upper) and $CSD_{Si/STO}$ (lower). The discussion includes increased bulk resistance ρ_{RT} – measured through ohmic Au pads (yellow pads in the figure) – and higher coercivity field (B_c) due to structural deformation along with lower magnetic ordering temperature (T_N) in CSD fabricated films on STO buffered silicon. All the films exhibited resistive switching –measured through Al (grey pads in the figure) and Au pads– but the switching ratio is higher and the phenomenon appears more stable in PLD film fabricated on STO substrate.

Interestingly, $CSD_{Si/STO}$ showed the most stable LRS state without significant decay in the retention. This is demonstrated by minimal statistical deviations from the median as depicted in Fig. 5 (d). The presented results in (c) and (d) represent the selected best result set. Indeed, the apparent impression was that the results for PLD_{STO} seemed the most consistent between various devices on the same GCMO sample, while other samples showed more variation in device performance. This was tested by measuring the characteristics of additional five identical device junctions for both PLD_{STO} and $CSD_{Si/STO}$. Although devices on PLD_{STO} showed some variation, all the devices showed distinctive LRS and HRS states, while none of the additional $CSD_{Si/STO}$-based devices showed RS performance. This confirms the impression stated that $CSD_{Si/STO}$-based devices showed inconsistent RS characteristics. However, similar inconsistencies were not apparent in CSD_{STO}.

4. Discussion

From the measurements, we also note an increasing trend in $\Delta\phi$ of GCMO phase when substituting PLD fabrication with CSD and STO substrates with Si/STO. Both of these changes were also accompanied by increased resistivity accordingly, while T_N

decreased when only STO was substituted. Additionally, all the samples showed RS characteristics, but the performance was inconsistent, especially in $CSD_{Si/STO}$, and PLD_{STO}-based devices appeared the most consistent in their RS performance. The Fig. 6 illustrates these remarks and the following discussion.

The structural changes have their response in ohmic conductive properties since structural defects induce charge scattering but also the disruption of Mn–O–Mn bonds could potentially alter the conduction in a perovskite manganite film [44, 45]. Although the spin-dependent double exchange conduction in GCMO is likely to have little to no effect at room temperature due to $T_C \approx 100\,K$ and the antiferromagnetic phase being predominant in $x = 0.8$, small polaronic hopping conduction, evidenced in GCMO at higher temperatures [26], is to be influenced by structural defects due to increased activation energy. Therefore, the correlation between structural defects and ohmic resistivity of GCMO phase appears as would be expected. In addition, the detail regarding the structural analysis is that while $CSD_{Si/STO}$ shows the highest $\Delta\phi$-value, the $\Delta\theta$-value, although being the highest, does not stand out from the respective value for PLD_{STO}. This seems to suggest that strain relaxation is not imminent despite the pronounced structural deformation, such as low-angle grain boundaries.

The disparity observed in films prepared via CSD, is not only manifested in the structural characteristics of the film but also in how it impacted the film's resistivity and compromised its memristive properties. Previous research has demonstrated the heightened sensitivity of the interface between STO and Si to re-crystallization temperature [46]. At temperatures as low as 500 °C, SrO desorption at the interface is initiated, leading to a discernible roughening of the film surface. Given the potential significance of such interface alterations, especially in the case of our thin STO layers with a mere thickness of 3–4 nm, we conducted preliminary tests, manipulating the crystallization temperature in the STO/Si substrate scenario.

As depicted in Fig. 7, the crystallization temperature significantly influences the in-plane and out-of-plane structural properties of GCMO thin films grown on a $CSD_{Si/STO}$ substrate. Notably, the full width at half maximum (FWHM) of the peak in the ϕ-direction reduces by approximately half as the crystallization temperature decreases from 750 °C to 600 °C. This reduction indicates a substantial enhancement in in-plane crystalline quality, characterized by a noticeably diminished prevalence of low-angle grain boundaries. Similarly, the improvement in out-of-plane crystallographic texture is even more pronounced, with the FWHM of the ω-scans decreasing to around a quarter. This suggests that at a lower temperature of 600 °C, the crystallized film exhibits a significantly longer lattice coherence length along the GCMO out-of-plane direction [47].

Despite the improved crystalline quality due to lower crystallization temperature in $CSD_{Si/STO}$ films, the device yield for RS is still not comparable to PLD fabricated devices on STO. We believe that this arises from the fact that STO-buffered Si substrates used in CSD might not provide a solid setting for device construction by a wire bonder. Indeed the resistance of the STO buffered silicon substrate is in the range of 1–10

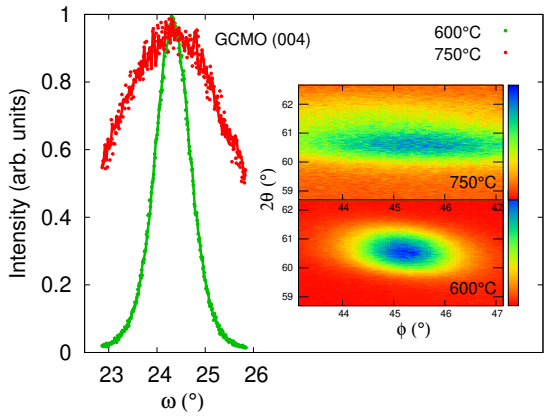

Figure 7: The normalized XRD rocking curves (ω-scans) of the GCMO (004) peaks measured from the GCMO films on $CSD_{Si/STO}$ substrate crystallized at different temperatures of 750 °C and 600 °C. The inset shows the GCMO (204) peaks as functions of 2θ and relative ϕ for the same films treated at 750 °C and 600 °C.

MΩ. This is likely to suppress the detection of any HRS state exceeding the substrate resistance, since an intrusion by Al wire short-circuiting over the GCMO layer directly to the substrate will act as a leakage path.

The phenomenon of resistive switching in manganite-based systems is seen to be linked to interfacial oxygen exchange between two acting electrodes [48, 49, 50, 51, 52, 53]. Our previous research demonstrates that epitaxial films are not a prerequisite for the resistive switching phenomenon in GCMO [40]. This is also suggested by the work conducted on various manganite-based devices reported in the literature [54, 55, 56, 57, 58]. Hence, the results showing resistive switching in all our samples here, despite the significant structural distortion in GCMO, are in line with previous reported results. Although a more careful device fabrication is needed to account for the low device yield, as a new accomplishment the current work clearly demonstrates that CSD-based GCMO fabrication is successful in developing memristive planar devices on multiple substrate materials. The phenomenon of resistive switching remains robust against structural distortion resulting from CSD. Notably utilizing buffered silicon substrates resulted in successful devices. With further device optimization by engineering capacitive device structures, we expect a significant improvement in device yield fabricated on the buffered silicon substrates. Fabricating devices on top of Si substrates is an important requirement for the seamless co-integration of this new technology with existing semiconducting fabrication facilities.

5. Conclusions

In conclusion, our findings highlight the critical importance of both the growth method and substrate-induced crystalline quality in shaping the performance of Al/GCMO/Au

memristor devices. Notably, memristor structures fabricated via pulsed laser deposition (PLD) on single crystal $SrTiO_3$ (STO) substrates consistently demonstrate superior crystalline quality, resulting in enhanced resistive switching properties. Conversely, structures produced using chemical solution deposition (CSD) and on silicon-based substrates exhibit compromised structural integrity, leading to increased resistance in the GCMO layer and weakened resistive switching behavior. These observations underscore the necessity of meticulously selecting growth methods and substrate materials to optimize memristor performance across diverse applications. Moreover, our discussion of underlying mechanisms provides valuable insights into the phenomena governing changes in resistive switching properties, thereby laying the groundwork for future advancements in memristor technology.

Acknowledgments

This project has received funding from the European Union's Horizon 2020 research and innovation programme under the Marie Skłodowska-Curie grant agreement No 101034371 as well as the Academy of Finland project 352802. The authors also acknowledge the Jenny and Antti Wihuri Foundation for financial support. Additionally, A. Antola acknowledges the Finnish Cultural Foundation and the University of Turku Graduate School (UTUGS) for their financial support.

References

[1] Kim S K and Popovici M 2018 *MRS Bulletin* **43** 334–339
[2] Ielmini D 2018 *Microelectronic Engineering* **190** 44–53
[3] Ielmini D and Wong H 2018 *Nature Electronics* **1** 333–343
[4] Zidan M A, Strachan J P and Lu W D 2018 *Nature Electronics* **1** 22–29
[5] Hickmott T W 1962 *J. Appl. Phys.* **33** 2669–2682
[6] Chua L 1971 *IEEE Transactions on Circuit Theory* **18** 507–519
[7] Zahoor F, Zulkifli T Z A and Khanday F A 2020 *Nanoscale Research Letters* **15** 90
[8] Waser R, Dittmann R, Staikov G and Szot K 2009 *Adv. Mater.* **21** 2632–2663
[9] Roy K, Jaiswal A and Panda P 2019 *Nature* **575** 607–617
[10] Moradi S and Manohar R 2019 *J. Phys. D Appl. Phys.* **52** 014003
[11] Maass W 2016 *Proceedings of the National Academy of Sciences* **113** 11387–11389
[12] Hong X L, Loy D J J, Dananjaya P A, Tan F, Ng C W and Lew W X 2018 *J. Mater. Sci.* **53** 8720–8746
[13] Sawa A 2008 *Materials Today* **11** 28–36
[14] Kim S, Park K, Hong K, Kim T H, Park J, Youn S, Kim H and Choi W Y 2024 *Adv. Mater. Technol.*
[15] Milozzi A, Ricci S and Ielmini D 2024 *Nat. Commun.* **15**
[16] Csontos M, Horst Y, Olalla N J, Koch U, Shorubalko I, Halbritter A and Leuthold J 2023 *Adv. Electron. Mater.* **9**
[17] Bagdzevicius S, Maas K, Boudard M and Burriel M 2022 *J Electroceram* 235–287
[18] Liu Q, Gao S, Xu L, Yue W, Zhang C, Kan H, Li Y and Shen G 2022 *Chem. Soc. Rev.* **51** 3341–3379
[19] Lashkare S, Chouhan S, Chavan T, Bhat A, Kumbhare P and Ganguly U 2018 *IEEE Electron Device Letters* **39** pp.484–487

[20] Kanegami N, Nishi Y and Kimoto T 2020 *Appl. Phys. Lett.* **116** 013501

[21] Ortega-Hernandez R, Coll M, Gonzalez-Rosillo J, Palau A, Obradors X, Miranda E, Puig T and Sune J 2015 *Microelectron. Eng.* **147** 37–40

[22] Miranda E, Acevedo W R, Rubi D, Lüders U, Granell P, né J S and Levy P 2017 *J. Appl. Phys.* **121** 205302

[23] Lähteenlahti V, Schulman A, Beiranvand A, Huhtinen H and Paturi P 2021 *ACS Appl. Mater. Interfaces* **13** 18365–18371

[24] Beiranvand A, Tikkanen J, Huhtinen H and Paturi P 2017 *J. Alloy Compd.* **720** 126–130

[25] Beiranvand A, Tikkanen J, Huhtinen H and Paturi P 2019 *J. Magn. Magn. Mater.* **469** 253–258

[26] Schulman A, Beiranvand A, Lähteenlahti V, Huhtinen H and Paturi P 2020 *J. Magn. Magn. Mater.* **498** 166149:1–6

[27] Beiranvand A, Liedke M O, Haalisto C, Lähteenlahti V, Schulman A, Granroth S, Palonen H, Butterling M, Wagner A, Huhtinen H and Paturi P 2022 *J. Phys. Cond. Mat.* **34** 155804

[28] Zidan M A, Fahmy H A H, Hussain M M and Salama K N 2013 *Microelectronics Journal* **44** 176–183

[29] Aguirre F L, Gomez N M, Pazos S M, Palumbo F, Suñé J and Miranda E 2021 *J. Low Power Electron. Appl.* **11** 9

[30] Paasonen V M M, Angervo I, Antola A, Huhtinen H and Paturi P 2024 *Thin Solid Films* (in press)

[31] Beiranvand A, Tikkanen J, Rautakoski J, Huhtinen H and Paturi P 2017 *Mater. Res. Express* **4** 036101

[32] Palonen H, Huhtinen H, Shakhov M A and Paturi P 2013 *Supercond. Sci. Technol.* **26** 045003:1–5

[33] Nyman M, Elovaara T, Tikkanen J, Majumdar S, Huhtinen H and Paturi P 2015 *Physics Procedia* **75** 1122

[34] Wu J and Leighton C 2003 *Phys. Rev. B* **67** 174408

[35] Nam D N H, Jonason K, Nordblad P, Khiem N V and Phuc N X 1999 *Phys. Rev. B* **59** 4189

[36] Li B, Yang L, Tian J Z, Wang X P, Zhu H and Endo T 2011 *J. Appl. Phys.* **109** 073922:1–5

[37] Beiranvand A, Liedke M O, Haalisto C, Lähteenlahti V, Schulman A, Granroth S, Palonen H, Butterling M, Wagner A, Huhtinen H and Paturi P 2021 *J. Phys. Cond. Mat.* **33** 255803

[38] Nogues J and Schulle I K 1999 *J. Magn. and Magn. Mater.* **192** 203–232

[39] Berkowitz A and Takano K 1999 *J. Magn. and Magn. Mater.* **200** 552–570

[40] Angervo I, Antola A, Schulman A, Huhtinen H and Paturi P 2024 *AIP Adv.* **14** 045309:1–9

[41] Lähteenlahti V, Schulman A, Huhtinen H and Paturi P 2019 *J. Alloys Compd.* **786** 84–90

[42] Jang J W, Park S, Burr G W, Hwang H and Jeong Y H 2015 *IEEE Electron Device Lett.* **36** 457–459

[43] Moon K, Fumarola A, Sidler S, Jang J, Narayanan P, Shelby R, Burr G, and Hwang H 2018 *IEEE Journal of the Electron Devices Society* **6** 146–155

[44] Nelson C S, Hill J P, Gibbs D, Rajeswari M, Biswas A, Shinde S, Greene R L, Venkatesan T, Millis A J, Yokaichiya F, Giles C, Casa D, Venkataraman C T and Gog T 2004 *J. Phys. Cond. Mat.* **16** 13

[45] Prellier W, Lecoeur P and Mercey B 2001 *J. Phys. Cond. Mat.* **13** R915

[46] Goncharova L V, Starodub D G, Garfunkel E, Gustafsson T, Vaithyanathan V, Lettieri J and Schlom D G 2006 *J. Appl. Phys.* **100** 014912:1–6

[47] Gauzzi A and Pavuna D 1995 *Appl. Phys. Lett.* **66** 1836–1838

[48] Asanuma S, Akoh H, Yamada H and Sawa A 2009 *Phys. Rev. B* **80** 235113

[49] Rozenberg M J, Sánchez M J, Weht R, Acha C, Gomez-Marlasca F and Levy P 2010 *Phys. Rev. B* **81** 115101

[50] Nian Y B, Strozier J, Wu N J, Chen X and Ignatiev A 2007 *Phys. Rev. Lett.* **98** 146403

[51] Kramer T, Scherff M, Mierwaldt D, Hoffmann J and Jooss C 2017 *Appl. Phys. Lett.* **110** 243502

[52] Liao Z, Gao P, Chen X B D and Zhang J 2012 *J. Appl. Phys.* **111** 114506

[53] Herpers A, Lenser C, Park C, Offi F, Borgatti F, Panaccione G, Menzel S, Waser R and Dittmann R 2014 *Adv. Mater.* **26** 2730

[54] Lau H K, Leung C W and Chan Y K 2009 *Phys. Status Solidi A* **206** 2182
[55] Solanki P, Vala M, Dhruv D, Bhatt S V and Kataria B 2022 *Surf. Interfaces* **35** 102474
[56] Liu X, Biju K P, MBourim E, Park S, Lee W, Shin J and Hwang H 2010 *Solid State Commun.* **150** 2231
[57] Li S L, Shang D S, Li J, Gang J L and Zheng D N 2009 *J. Appl. Phys.* **105** 033710
[58] Borgatti F, Park C, Herpers A, Offi F, Egoavil R, Yamashita Y, Yang A, Kobata M, Kobayashi K, Verbeeck J, Panaccione G and Dittmann R 2013 *Nanoscale* **5** 3954